PUBLICATIONS OF THE ASTRONOMICAL SOCIETY OF THE PACIFIC, **127**:437–444, 2015 May

An Achromatic Focal Plane Mask for High-Performance Broadband Coronagraphy

K. NEWMAN,[1,2] O. GUYON,[1,3] K. BALASUBRAMANIAN,[4] R. BELIKOV,[2] N. JOVANOVIC,[3] F. MARTINACHE,[3] AND D. WILSON[4]

Received 2014 December 01; accepted 2015 February 24; published 2015 April 1

ABSTRACT. Developments in coronagraph technology are close to achieving the technical requirements necessary to observe the faint signal of an Earth-like exoplanet in monochromatic light. An important remaining technological challenge is to achieve high contrast in broadband light. Coronagraph bandwidth is largely limited by chromaticity of the focal plane mask, which is responsible for blocking the stellar PSF. The size of a stellar PSF scales linearly with wavelength; ideally, the size of the focal plane mask would also scale with wavelength. A conventional hard-edge focal plane mask has a fixed size, normally sized for the longest wavelength in the observational band to avoid starlight leakage. The conventional mask is oversized for shorter wavelengths and blocks useful discovery space. We present a new focal plane mask which operates conceptually as an opaque disk occulter, but uses a phase mask technique to improve performance and solve the "size chromaticity" problem. This achromatic focal plane mask would maximize the potential planet detection space without allowing starlight leakage to degrade the system contrast. Compared with a conventional opaque disk focal plane mask, the achromatic mask allows coronagraph operation over a broader range of wavelengths and allows the detection of exoplanets closer to their host star. We present the generalized design for the achromatic focal plane mask, implementation within the Subaru Coronagraph Extreme Adaptive Optics instrument, and laboratory results which demonstrate the size-scaling property of the mask.

Online material: color figures

1. INTRODUCTION

Coronagraphy is a technique for directly imaging extrasolar planets by blocking the light from a star so that the faint light of a nearby exoplanet can be observed. In a typical coronagraph architecture, the input pupil is focused onto a focal plane mask, hereafter referred to as "mask," which is designed to eliminate the starlight. A Lyot stop is then used to control the diffraction introduced by the mask. Pupil plane apodization can be used in combination with an occulting mask to achieve a high contrast PSF, as shown in the Apodized Pupil Lyot Coronagraph (Soummer et al. 2003a) and the high throughput Phase-Induced Amplitude Apodization (PIAA) Coronagraph (Guyon 2003). The mask may alternatively be designed to provide a phase shift to a portion of the starlight and force the shifted starlight to interfere destructively with the un-shifted starlight. The phase mask coronagraph (Roddier & Roddier 1997) uses a circular phase plate to produce a π phase shift in the core of the stellar image. The Four-Quadrant Phase Mask (Rouan et al. 2000) is a binary mask with alternating sections that produce 0 and π phase shift. The Optical Vortex Coronagraph (Palacios 2005) uses a diffractive optical element with a purely azimuthal phase ramp to produce a smooth gradient phase profile in the azimuthal direction. The Annular Groove Phase Mask (Mawet et al. 2005) induces an achromatic optical vortex by using a subwavelength zero-order grating. The Dual-Zone Phase Mask (Soummer et al. 2003b) consists of two concentric phase masks where the thickness of each is optimized to null starlight over a large bandwidth. Phase masks generally allow planet detection closer to the star and can achieve higher contrast when compared with the opaque occulting masks. However, phase masks can be particularly sensitive to manufacturing errors and instrument alignment errors. One advantage of using an opaque occulting mask is the simple manufacturing and alignment. In this article, we propose a new mask which operates conceptually as an opaque disk occulter, but uses a phase mask technique to improve performance and solve the "size chromaticity" problem, namely, the fact that the size of a telescope point spread function (PSF) illuminating a coronagraphic mask will scale with wavelength, but coronagraphic masks of course stay fixed in size.

The size of a typical occulting disk is designed to match the stellar PSF size at the longest wavelength in the coronagraph

[1] College of Optical Sciences, University of Arizona, 1630 E. University Blvd, Tucson, AZ 85721; knewman@email.arizona.edu.

[2] NASA Ames Research Center, Bldg 245-144, Moffett Field, CA 94035.

[3] National Astronomical Observatory of Japan (NAOJ), Subaru Telescope, 650 North A'Ohoku Pl, Hilo, HI 96720.

[4] NASA Jet Propulsion Laboratory, California Institute of Technology, 4800 Oak Grove Drive, Pasadena, CA 91109.

bandwidth, therefore blocking potential planet detection space from the shorter wavelengths. The alternative is to reduce the size of the disk; however, this allows starlight at longer wavelengths to pass around the mask and decreases the contrast. The size of an ideal mask would scale linearly with wavelength to match the size of the stellar PSF. This achromatic focal plane mask would maximize the potential planet detection space without allowing starlight leakage to degrade the system contrast. Compared with a conventional opaque disk mask, the achromatic mask allows coronagraph operation over a broader range of wavelengths and allows the detection of exoplanets closer to their host star (Newman et al. 2013, 2014).

In this article, we present a design for an achromatic focal plane mask based on the diffractive optical filtering technique (Belikov & Solgaard 2003). In § 2, we describe the design of a size-scaling achromatic mask for the Subaru Coronagraph Extreme Adaptive Optics (SCExAO) instrument (N. Jovanovic et al. 2014, in preparation). The same design principles can be applied to create an achromatic mask for other coronagraphs. In § 3, we show results from laboratory testing that demonstrate the advantages of an achromatic mask compared with a conventional hard-edge opaque mask.

2. ACHROMATIC FOCAL PLANE MASK DESIGN

Achromatic masks can be designed as substitutes for any coronagraph normally using a hard-edge mask. This paper focuses on a specific mask that was designed, manufactured, and tested for SCExAO (N. Jovanovic et al. 2014, in preparation), an extreme adaptive optics (ExAO) type instrument installed at the Subaru Telescope. Several features of the instruments drive specifics of the mask design.

The mask was designed to be used in the H-band (1.5–1.8 μm) with a pupil apodized using the PIAA technique (Guyon 2003). The main consequence of this setup is that when it reaches the focal plane, the beam has an equivalent focal ratio $f/65$. Any high-performance coronagraph requires fine pointing control. On SCExAO, this is achieved via a closed-loop system monitoring the light rejected by the coronagraph, forming a subsystem called the coronagraphic low-order wavefront sensor (CLOWFS; Guyon et al. 2009; Vogt et al. 2011). Figure 1 illustrates the way this approach is implemented on SCExAO.

In a coronagraph, the mask diffracts light of the on-axis bright source away from the center of the geometric pupil. This light needs to be blocked by a separate mask, usually located in a reimaged pupil plane after the mask, a component called the Lyot-stop. In SCExAO, the Lyot-stop is reflective so that the light rejected by it can be reimaged onto a camera. CLOWFS monitors this image and uses it to drive a servo-loop that efficiently stabilizes the tip-tilt and other low-order modes such as focus and astigmatism (Singh et al. 2014). Our mask design offers the opportunity to further improve the sensitivity of this CLOWFS because the mask structure influences the spatial distribution of the light in the Lyot-plane. The reflective Lyot-plane stop within SCExAO is a flat mirror with a circular hole cut through the center. Light that passes through the center hole of the Lyot stop is potential planet detection light, and it continues propagating toward the science camera. The starlight that is diffracted by the mask is incident upon the Lyot stop outside of the center hole, on the reflective area of the Lyot stop.

2.1. Mask Structure

The effective size of the mask is designed to scale with wavelength throughout the system bandwidth. We will define the system bandwidth as spanning from the shortest wavelength ($\lambda_{\rm min}$) to the longest wavelength ($\lambda_{\rm max}$). The mask pattern, shown in Figure 2, is etched into a Silicon wafer, and consists of a central cone-shaped structure surrounded by an azimuthally periodic binary pattern. The cone is designed to reject all starlight incident on it as if it was an opaque disk, except instead of blocking the light directly, it diffracts it outside the pupil to be blocked by the Lyot-stop. Geometrically, the cone structure acts exactly like a conical lens. The radius of the cone (r_c) is set to the desired

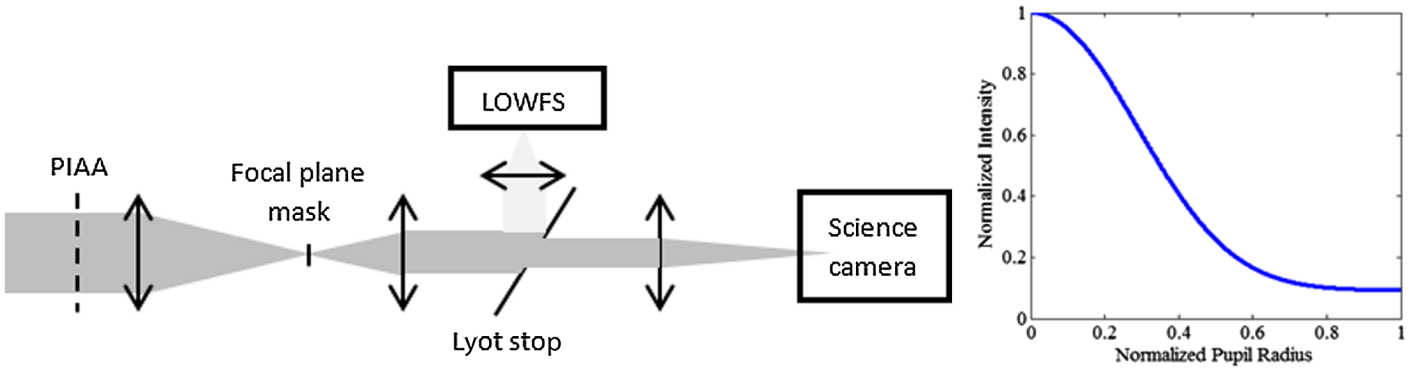

FIG. 1.—Schematic of SCExAO instrument (*left*) and intensity profile in the pupil plane after PIAA (*right*). The achromatic focal plane mask diffracts starlight onto a partially reflective Lyot stop which is then used in a low-order wavefront sensor. Planet light is passed by the focal plane mask and imaged onto the science camera. See the electronic edition of the *PASP* for a color version of this figure.

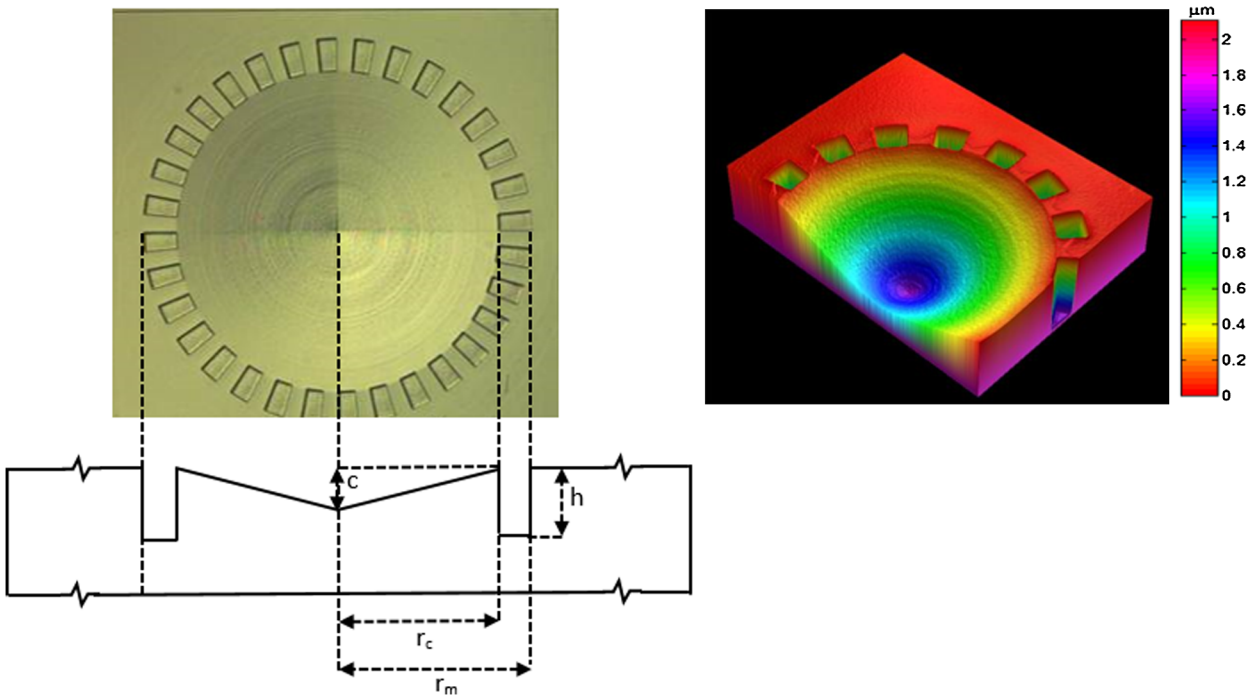

FIG. 2.—A microscope image of a mask fabricated at NASA JPL Microdevices Laboratory, along with a diagram to define geometric parameters of the mask (*left*). Isometric view of mask profilometry (*right*). See the electronic edition of the *PASP* for a color version of this figure.

size of the occulter for a particular coronagraph design at $\lambda_{\rm min}$. The desired size varies based on apodization profile, desired inner working angle (IWA), and desired contrast, but a typical occulter would be sized for 0.5–2λ/D. The outer radius of the mask (r_m) is set to the desired size of the occulter at $\lambda_{\rm max}$. The size of the stellar PSF scales with wavelength, so to keep a consistent size of the mask relative to wavelength, r_m scales with the system bandwidth. For example, a typical coronagraph bandwidth is 20%, so $\lambda_{\rm max}$ is 20% larger than $\lambda_{\rm min}$; in this case, r_m should be 20% larger than r_c.

There is a binary pattern around the outer edge of the mask which is similar in structure to the teeth of a circular gear. The relative height difference between adjacent teeth (h) produces a phase shift and causes the light to diffract. We describe in § 2.2 how to tune the parameter h to produce a phase shift that allows the size of the mask to scale with wavelength. The end result is that the region with binary structure is effectively opaque to long-wavelengths, yet transparent to short wavelengths, so that the size of the mask effectively scales with wavelength. The binary pattern region diffracts short wavelength light inside the Lyot stop opening, allowing it to pass to the science camera, but starlight at long wavelengths is diffracted outside the Lyot stop, rejecting it from the system.

There are four degrees of freedom in the mask design: the radius of the cone, the slope of the cone, the system bandwidth, and the number of segments in the binary pattern. Each of these degrees of freedom has an impact on the system performance which can be described by the diffraction pattern of light in the Lyot plane. Light incident upon the central cone of the mask is always diffracted into a ring in the Lyot plane. The radius of the cone (r_c) determines the amount of the stellar PSF at $\lambda_{\rm min}$ that is diffracted, and therefore blocked from the science camera. The radius of the cone should be set to match the desired size of the occulter at $\lambda_{\rm min}$. The angle of the cone, computed by the ratio c/r_c, determines the radial position of diffracted light in the Lyot plane. A steeper angle moves the starlight further from the optical axis, and a shallow angle moves the starlight closer to the optical axis. If one is only concerned with removing the starlight from the system, then a steep angle within manufacturing limits would be appropriate. However, the rejected starlight can be useful for CLOWFS, so we adjust the angle of the cone to send the rejected starlight into collecting optics for the CLOWFS. In the case of SCExAO, the starlight is collected in a tight circular area directly surrounding the outer extent of the Lyot mask.

Light at longer wavelengths that is incident upon the periodic binary structure is also diffracted into a ring in the Lyot plane, centered on the optical axis. The number of segments in the binary structure (and therefore the frequency between adjacent segments) determines the radial position of the diffracted light in the Lyot plane. An increase in the number of binary segments will move the diffracted light further from the optical axis. To simply remove the diffracted starlight from the system, a high number of segments is appropriate within manufacturing limits.

However, this diffracted starlight can also be useful for CLOWFS, so for SCExAO, we adjust the number of segments to send the starlight into a tight ring surrounding the outer extend of the Lyot stop. A typical number of segments is between 14 and 30. The SCExAO mask is optimized to position diffracted light between 4.5 and 12.5 mm radial distance from the optical axis in the Lyot plane, which is 1.0 and 2.8 pupil radii, respectively, and corresponds to the reflective region of the Lyot stop. The only remaining parameter of the mask design is the relative depth between adjacent segments of the binary structure, h. The segment depth, which creates a phase shift between adjacent segments, is a calculated parameter based on the system bandwidth.

2.2. Phase Shift

The mask is modeled as a pure phase mask (i.e., amplitude transmission is 1). Any space not occupied by the profile of the silicon mask is occupied by air, so the effective phase shift of the mask is given relative to the phase shift that would have occurred if the mask were made of air. A generic calculation of phase shift can easily be achieved for any part of the mask, but here we focus on the periodic binary pattern at the edge of the mask because it determines the achromatic size-scaling property of the mask. The relative phase shift ($\Delta\Phi$) between adjacent binary segments is given in equation (1) as a function of the segment depth (h) and the refractive index of silicon (n_{Si}) for a particular wavelength (λ). The phase shift is computed in units of wavelengths. We make the approximation $n_{\rm air} = 1.000$ because any further significant digits of the mask thickness usually amount to subnanometer levels that cannot be accurately manufactured.

$$\Delta\Phi = (n_{Si}(\lambda) - 1) * \frac{h}{\lambda} \quad (1)$$

The Lyot stop forces interference between adjacent segments in the binary structure. The goal is to create constructive interference at the shortest wavelength in the observing band, and destructive interference at the longest wavelength in the observing band. For the SCExAO mask, we compute h for a 20% bandwidth in the H-band, where $\lambda_{\rm min} = 1.5$ μm and $\lambda_{\rm max} = 1.8$ μm. For $h = 1.81$ μm, there is a nearly ideal relationship between wavelength and phase shift: at $\lambda_{\rm min}$ the phase shift is 2.995 wavelengths, which is close to a 6π phase shift, and at $\lambda_{\rm max}$ the phase shift is 2.475 wavelengths, which is close to a 5π phase shift. Therefore, adjacent segments in the binary structure produce constructive interference for $\lambda_{\rm min}$, causing that part of the mask to behave as if it was transparent, and destructive interference for $\lambda_{\rm max}$, causing that part of the mask to behave as if it was opaque. As shown in Figure 3, the relationship between wavelength and phase shift is nearly linear within the H-band. This results in a mask with an effective size that scales monotonically with wavelength. We could create an achromatic mask for any of the slopes in Figure 3 that are highlighted in green, because there is constructive interference at $\lambda_{\rm min}$ and destructive interference at $\lambda_{\rm max}$. The region in Figure 3 that is

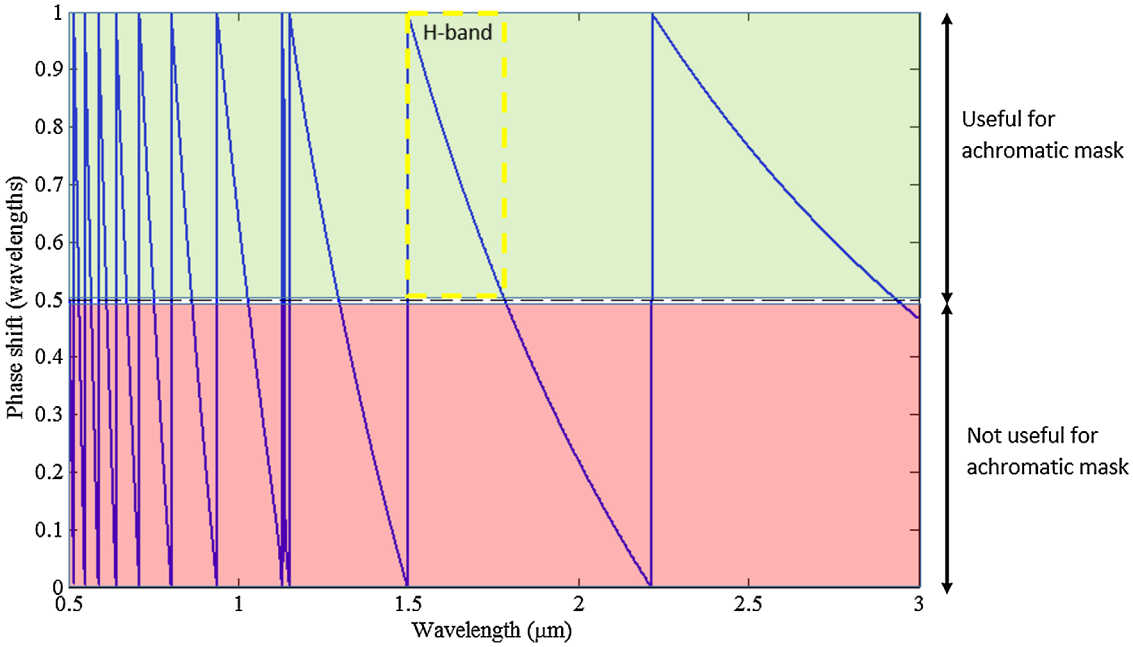

FIG. 3.—Phase shift produced by adjacent cells in the achromatic mask binary pattern as a function of wavelength for $h = 1.81$ μm. The phase is wrapped back to zero for shifts greater than one wavelength. Within the H-band (*dashed yellow box*), the phase shift is nearly linear. See the electronic edition of the *PASP* for a color version of this figure.

highlighted in red has slopes with the opposite effect compared with what is useful for an achromatic mask, destructive interference at $\lambda_{\min}$, and constructive interference at $\lambda_{\max}$. The phase curves keep a similar pattern, but shift for different values of h and for materials with different refractive indices. However, there is clearly a limit to the bandwidth over which this mask design can produce an effective phase shift that scales with wavelength; it would be difficult to produce an achromatic design with greater than 20% bandwidth.

2.3. Fabrication

The mask design contains small features that require precise nanofabrication. The NASA Jet Propulsion Laboratory (Microdevices Laboratory) has extensive experience making focal plane masks using various techniques (Balasubramanian 2013). They fabricated the achromatic masks using gray-scale electron beam lithography and plasma transfer etching. An array of masks were etched onto a silicon substrate with H-band antireflection coating on one side. It is beneficial to have masks with various sizes available on the same substrate, so we created four scaled versions of the same mask design with $r_c = 130$, 163, 203, and 254 μm, which represent approximately $1\lambda/D$, $1.25\lambda/D$, $1.56\lambda/D$, and $1.95\lambda/D$ for the apodized beam described above, respectively. Balasubramanian et al. (2013) provide a more detailed description of the mask fabrication process.

3. RESULTS

3.1. Characterization of Size-Scaling with Wavelength

We can verify the size-scaling principle of the focal plane mask as a function of wavelength using simulations. For the first simulation, we create an apodized PSF which models the stellar PSF that is achieved in an actual coronagraph. At first, the PSF is centered on the mask, and the mask is blocking most of the starlight as it would in normal coronagraph operation. The PSF is then moved off axis in regular increments to simulate an off-axis source at various distances relative to the center of the mask. We measure the throughput of the PSF at each increment and calculate the point at which the throughput reaches 50%, known as the IWA. The IWA is considered to be the effective edge of the mask. The simulation is repeated for the shortest, middle, and longest wavelengths within the design bandwidth. Each throughput curve is normalized relative to the maximum throughput that is achieved when the PSF is completely unobstructed by the mask. Results are shown in Figure 4 for the $1\lambda/D$ achromatic mask designed for SCExAO, which has $r_c = 130$ μm and $r_m = 156$ μm, and compared with a hard-edge mask with radius 156 μm. This represents a typical situation where the hard-edge mask is sized for the longest wavelength in the observing bandwidth.

For both types of focal plane mask, the throughput is low when the mask is directly occulting the PSF. The throughput increases near the edge of the mask, and reaches a maximum

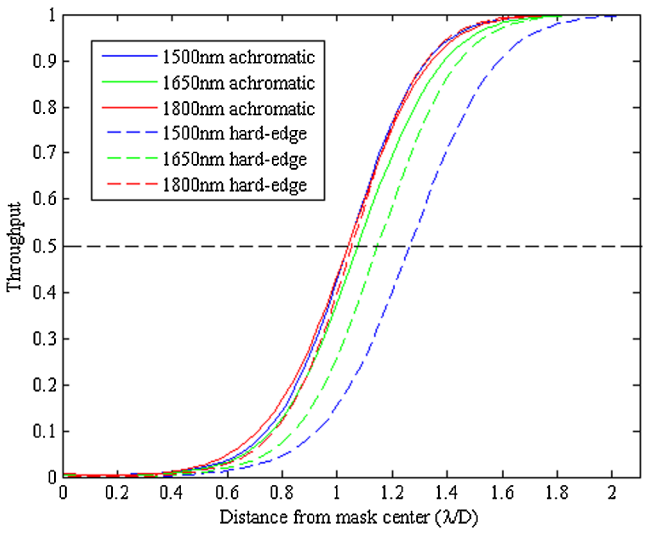

FIG. 4.—First simulation of the size-scaling property of the achromatic mask as a function of wavelength (*solid lines*). Results are compared to a conventional hard-edged mask (*dashed lines*). We measure throughput of an off-axis source and compare IWA for different wavelengths. See the electronic edition of the *PASP* for a color version of this figure.

when the PSF is no longer occulted by the mask. For the achromatic mask, the IWA is at nearly the same location for all wavelengths (in units of λ/D). Over the entire 20% observational bandwidth, the effective size of the mask deviates by only 2.8% in units of λ/D. If the mask could provide a perfectly linear phase shift as a function of wavelength over the entire bandwidth, the chromatic dispersion would be 0%. However, as shown in Figure 3, the phase shift relationship is not exactly linear, and does not provide perfect destructive interference at $\lambda_{\max} = 1.8$ μm. In this simulation, the maximum deviation actually occurs for the middle wavelength. Despite the imperfect phase shifts, the achromatic mask provides a clear advantage over a hard-edge mask. For the conventional hard-edge opaque mask, the IWA scales by 20%. This is an expected result for a 20% bandwidth because the mask has a fixed size.

A similar simulation is easier to replicate within the SCExAO instrument. For this second simulation, the mask and the PSF remain on-axis as they would in normal coronagraph operation. In this case, we measure the intensity of the residual light as a function of distance relative to the center of the mask, which is also the center of the PSF. We intentionally use a PSF that is oversized with respect to the mask so that there is significant light leakage around the edge of the mask. The PSF is apodized, so the intensity of the light leakage decreases with distance relative to the center of the mask. Therefore, the highest intensity of the light leakage occurs directly after the edge of the mask, and we can use this fact to identify where the edge of the mask is located. The experiment is repeated for different wavelengths, and we expect to see behavior that is similar to the effects shown in Figure 4. Each intensity curve is normalized relative to the

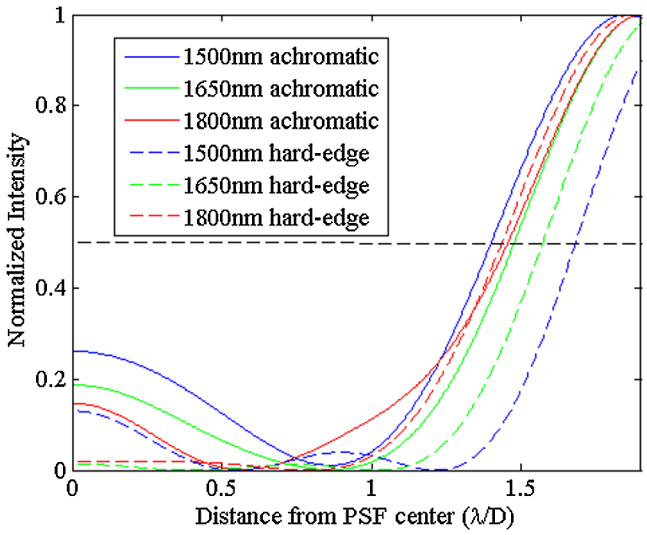

FIG. 5.—Second simulation of the size-scaling property of the achromatic mask as a function of wavelength (*solid lines*). Results are compared to a conventional hard-edged mask (*dashed lines*). See the electronic edition of the *PASP* for a color version of this figure.

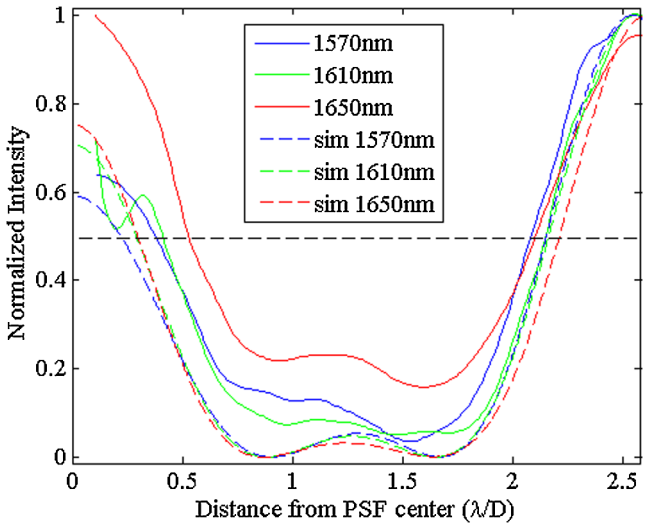

FIG. 6.—Intensity as a function of distance from the center of the mask in measurement (*solid lines*) and simulation (*dashed lines*) for various wavelengths. The location of intensity increase, representing the effective edge of the mask, scales with wavelength. See the electronic edition of the *PASP* for a color version of this figure.

greatest intensity within the curve. This simulation does not exactly measure throughput because the source remains on-axis. However, we can use the point of 50% maximum intensity of light leakage as a sort of "modified inner working angle" (mIWA) to compare the location of the edge of the mask for different wavelengths. Results are shown in Figure 5 for the $1\lambda/D$ achromatic mask compared with a hard-edge mask with radius 156 μm.

The intensity curves in Figure 5 have a similar profile compared with the throughput curves of the first simulation shown in Figure 4. One noticeable difference is that the intensity at zero distance relative to the mask center is much higher. This occurs because we are measuring light leakage, which has far less intensity than the unobstructed PSF that is used for normalization of the throughput profiles. Another noticeable difference is that the mIWA occurs at a slightly greater distance than the IWA. Again, this is due to the fact that the light leakage reaches a maximum at a distance slightly beyond the edge of the mask. In this simulation, over the entire 20% observational bandwidth, the mIWA deviates by only 3.9% in units of λ/D. For the conventional hard-edge opaque mask, the mIWA scales by 17%. The mIWA dispersion numbers are close to the IWA dispersion, but differ slightly because the source remains on-axis. We can use this experiment to clearly demonstrate the size-scaling property of the achromatic mask. The achromatic mask has an advantage over the hard-edge mask for observing exoplanets because the achromatic mask is not oversized for short wavelengths in the observational band.

We completed the same experiment that was described in the second simulation using a broadband supercontinuum source within SCExAO. To select only a narrow range of wavelengths at a time, we used bandpass filters centered at 1570, 1610, and 1650 nm wavelengths, each with FWHM of 12 nm. Figure 6 shows the resulting intensity measurements as the $r_c = 203$ μm achromatic mask was occulting the apodized PSF, along with a simulation for comparison. Results of the simulation are somewhat different than those presented in Figure 5 because they include parameters that are specific to the SCExAO optical layout. Unfortunately, the signal-to-noise ratio of the measurement was somewhat low due to the maximum output power of the supercontinuum source. However, we can identify features within the intensity curves that indicate the size-scaling effect of the achromatic mask. The mIWA dispersion is 2.8% in simulation and 3.2% in measurement, both of which are far less than what we would expect for a hard-edge mask. This is an important result because it shows that the size of the achromatic mask scales with wavelength.

3.2. Performance in Coronagraph

The first step to verify the operation of a focal plane mask for coronagraphy is to test its response to monochromatic light. We simulated a stellar point source within SCExAO by using a 1570 nm laser diode directed through an optical fiber. The simulated stellar PSF was apodized using PIAA lenses and focused onto the $r_c = 254$ μm mask. The science camera image shown in Figure 6 was recorded while the mask was blocking the source PSF. Images for the other three mask sizes show the same features, but have a different sized dark zone in the center of the image that corresponds to the size of the mask. The color scale represents contrast in the focal plane relative to the highest intensity pixel in an unobstructed PSF. The average contrast

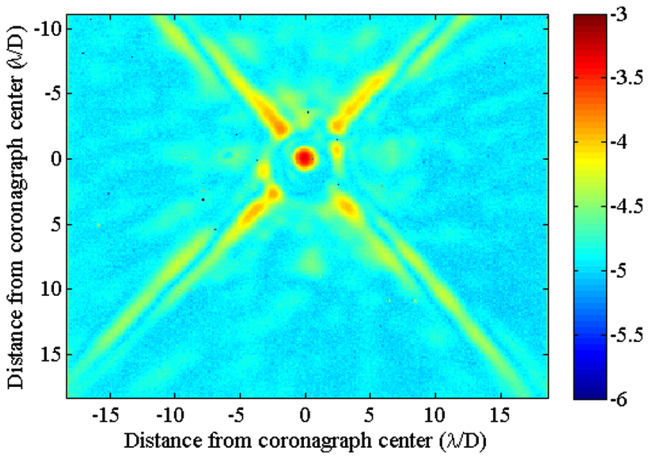

FIG. 7.—Image of focal plane mask contrast recorded using the SCExAO internal calibration source. The color scale is logarithmic and spans 4 orders of magnitude. See the electronic edition of the *PASP* for a color version of this figure.

between 3.8 and $7.7\lambda/\mathrm{D}$ distance from the center of the coronagraph is $1.47 * 10^{-5}$. From simulations, we expect to achieve an average contrast of $4.26 * 10^{-8}$ within the same boundaries. The brightness of the central peak is close to what we expect in simulation, but the diffraction spikes and system aberrations degrade the contrast further from the center of the coronagraph. The raw contrast presented in this article is without the use of wavefront control, but we plan to utilize wavefront control in future iterations to achieve deeper contrast.

We observe two important features in Figure 7 that degrade the contrast: a central spot and four diffraction spikes. We expect to see a Poisson-like spot located at the center of the image corresponding to the location directly behind the mask, and indeed, we observe this spot. However, the intensity of the spot is much greater than what we would expect from Poisson effects alone. In addition to the Poisson-like spot, manufacturing limits at the peak of the cone structure of the mask produce a flat surface that allows a small portion of the PSF to pass unobstructed. Unfortunately, the flat surface occurs at the point of greatest intensity of the PSF and produces a bright spot behind the center of the mask. We plan to mitigate this effect in the future by making a small portion of the center of the mask opaque.

The four diffraction spikes are caused by the support beams of the secondary mirror of the Subaru Telescope. When testing with the SCExAO internal calibration source, we included a pupil plane mask to simulate the effects of the Subaru Telescope central obscuration and support beams. However, we did not create a pupil plane mask to block the Subaru support beams after PIAA remapping. This is a major cause of light leakage into the science camera, and hence, the support beams are clearly visible in the images. Diffraction from the support beams degrades contrast over the entire image. Other blotches of light in the image are speckles caused by imperfections in the optical components, and these speckles further degrade the contrast. Speckles can be corrected using active wavefront control methods such as "speckle nulling" (Trauger et al. 2004), or EFC (Give'on et al. 2007); however, these procedures were not utilized for testing the masks. We plan to achieve better contrast by installing a modified pupil plane stop to block diffracted light from the support beams and using speckle nulling to eliminate residual speckles.

As we discussed in § 2.1, the focal plane mask was designed to diffract starlight into a ring structure in the Lyot plane so that it can be rejected by the coronagraph and used with CLOWFS. Ideally, the vast majority of the starlight would be diffracted into a tight ring on the Lyot stop mirror as shown in the simulation in Figure 8. The dashed white circle in Figure 8 marks the extent of the hole within the Lyot plane mirror, which is 0.56 pupil radii in size, and any light falling within this region is allowed to pass to the science camera. Our experimental data shows the same ring structure, but there is far more starlight remaining within the encircled region, which is caused by diffraction from the central obscuration and secondary support beams in the

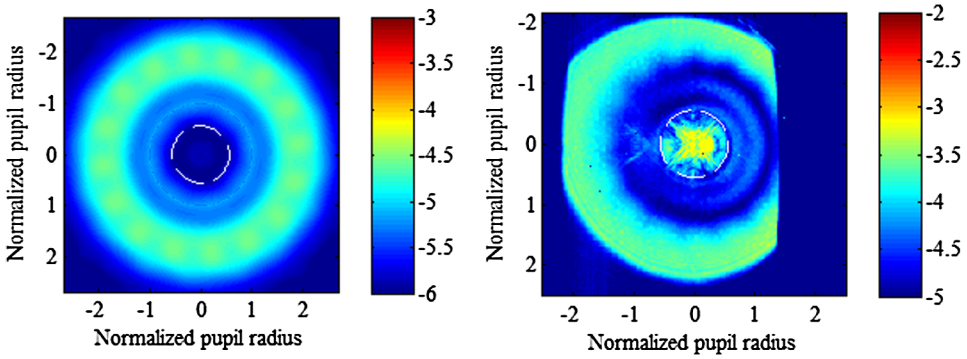

FIG. 8.—Simulation (*left*) and measured image (*right*) of starlight diffraction pattern in the Lyot plane. The logarithmic color scale spans 3 orders of magnitude and represents contrast relative to the maximum intensity of an unobstructed PSF. The scale for the measured image is offset by an order of magnitude relative to the simulated scale. See the electronic edition of the *PASP* for a color version of this figure.

telescope pupil. Only 0.41% of the starlight is allowed to pass through the Lyot stop, but this is enough to cause degradation of the contrast at the science camera. We can also see some vignetting in the measured Lyot plane image due to opto-mechanical mounts; however, this does not affect the operation of the mask or CLOWFS.

4. CONCLUSION

We have developed an achromatic focal plane mask for exoplanet-imaging coronagraphy, where the effective size of the mask scales with wavelength to match the size of the stellar PSF. The mask is meant to be a substitute for a conventional hard-edge opaque mask, and can be implemented into a coronagraph without any further changes to the system. The mask retains the operational simplicity of an opaque disk occulter, but utilizes the phase-shifting properties of a phase mask to create a size-scaling effect. The size-scaling technique is based on optical diffractive filtering in the Lyot plane, and the discarded starlight is utilized for CLOWFS. Compared with a conventional hard-edge mask, the achromatic mask allows greater throughput of an exoplanet at the shorter wavelengths of the system bandwidth. This increases the potential planet discovery space, and allows planets to be detected closer to their host stars. Laboratory measurements confirm the size-scaling effect of the mask. Of course, the achromatic mask is only useful if it can obtain a contrast level that is comparable or superior to an equivalent opaque occulting disk. We plan to demonstrate deep contrast with the mask while using wavefront control.

This work was supported in part by the National Aeronautics and Space Administration's Ames Research Center, as well as the NASA Astrophysics Research and Analysis (APRA) program through solicitation NNH09ZDA001N-APRA at NASA's Science Mission Directorate. It was carried out at the NASA Ames Research Center, Subaru Telescope, and Stanford Nanofabrication Facility. Any opinions, findings, and conclusions or recommendations expressed in this article are those of the authors and do not necessarily reflect the views of the National Aeronautics and Space Administration. This work was also supported by a NASA Space Technology Research Fellowship.

REFERENCES

Balasubramanian, K., Wilson, D., White, V., Muller, R., Dickie, M., Yee, K., Ruiz, R., Shacklan, S., et al. 2013, Proc. SPIE, 8864
Belikov, R., & Solgaard, O. 2003, Opt. Lett., 28, 6
Give'on, A., Kern, B., Shaklan, S., Moody, D., & Pueyo, L. 2007, Proc. SPIE, 6691
Guyon, O. 2003, A&A, 404, 397
Guyon, O., Matsuo, T., & Angel, R. 2009, ApJ, 693, 75–84
Mawet, D., Riaud, P., Absil, O., & Surdej, J. 2005, ApJ, 633, 1191–1200
Newman, K., Belikov, R., Guyon, O., Balasubramanian, K., & Wilson, D. 2013, Proc. SPIE, 8864
Newman, K., Belikov, R., Pluzhnik, E., Balasubramanian, D., & Wilson, D. 2014, Proc. SPIE, 9151, 216
Palacios, D. 2005, Proc. SPIE, 5905
Roddier, F., & Roddier, C. 1997, PASP, 109, 815
Rouan, D., Riaud, P., Boccaletti, A., Clenet, Y., & Labeyrie, A. 2000, PASP, 112, 1479–1486
Singh, G., Martinache, F., Baudoz, P., Guyon, O., Matsuo, T., Jovanovic, N., & Clergeon, C. 2014, PASP, 126, 940, 586–594
Soummer, R., Aime, C., & Falloon, P. 2003a, A&A, 397, 1161
Soummer, R., Dohlen, K., & Aime, C. 2003b, A&A, 403, 1, 369–381
Trauger, J., Burrows, C., Gordon, B., Green, J., Lowman, A., Moody, D., Niessner, A., Shi, F., et al. 2004, Proc. SPIE, 5487
Vogt, F., Martinache, F., Guyon, O., Yoshikawa, T., Yokochi, K., Garrel, V., & Matsuo, T. 2011, PASP, 123, 1434